

Turbulent characteristics of a shallow wall-bounded plane jet: experimental implications for river mouth hydrodynamics

JOEL C. ROWLAND¹ †, MARK T. STACEY²
AND WILLIAM E. DIETRICH³

¹Department of Geological and Environmental Sciences, Stanford University, Stanford, CA 94305, USA

²Department of Civil and Environmental Engineering, University of California, Berkeley, CA 94720, USA

³Department of Earth and Planetary Science, University of California, Berkeley, CA 94720, USA

(Received 25 March 2008 and in revised form 13 January 2009)

Jets arising from rivers, streams and tidal flows entering still waters differ from most experimental studies of jets both in aspect ratio and in the presence of a solid bottom boundary and an upper free surface. Despite these differences, the applicability of experimental jet studies to these systems remains largely untested by either field or realistically scaled experimental studies. Here we present experimental results for a wall-bounded plane jet scaled to jets created by flow discharging into floodplain lakes. A characteristic feature of both our prototype and experimental jets is the presence of large-scale meandering turbulent structures that span the width of the jets. In our experimental jets, we observe self-similarity in the distribution of mean streamwise velocities by a distance of six channel widths downstream of the jet outlet. After a distance of nine channel widths the velocity decay and the spreading rates largely agree with prior experimental results for plane jets. The magnitudes and distributions of the cross-stream velocity and lateral shear stresses approach self-preserving conditions in the upper half of the flow, but decrease in magnitude, and deviate from self-preserving distributions with proximity to the bed. The presence of the meandering structure has little influence on the mean structure of the jet, but dominates the jet turbulence. A comparison of turbulence analysed at time scales both greater than and less than the period of the meandering structure indicates that these structures increase turbulence intensities by 3–5 times, and produce lateral shear stresses and momentum diffusivities that are one and two orders of magnitude greater, respectively, than turbulence generated by bed friction alone.

1. Introduction

Jet theory has been used extensively to predict the turbulent discharge of rivers, streams and tidal inlets into quiescent bodies of water (e.g. Bates 1953; Borichansky & Mikhailov 1966; Wright & Coleman 1974; Ozsoy 1977; Joshi 1982; Kostaschuk 1985; Syvitski *et al.* 1998; Izumi, Tanaka & Date 1999, to list a few). While useful, this theory is not well supported with either field data (Bates 1953; Wright & Coleman

† Present address: Earth and Environmental Sciences Division, Los Alamos National Lab, Los Alamos, NM 87545, USA. Email address for correspondence: jrowland@lanl.gov

1974; Kostaschuk 1985; Old & Vennell 2001) or realistically scaled experimental studies. At river mouths and tidal inlets, turbulent mixing with the receiving waters is considered restricted to the vertical margins of the outflow due to contact with the bed at the base and the free water surface at top of the outflow. In this respect, river mouths and tidal inlets have generally been considered analogous to wall-bounded two-dimensional or plane jets (e.g. Bates 1953; Wright & Coleman 1974; Wright 1977).

In previous experimental work on bounded plane jets (e.g. Foss & Jones 1968; Holdeman & Foss 1975; Giger, Dracos & Jirka 1991; Dracos, Giger & Jirka 1992), the vertical dimension of the jet outlet exceeded the horizontal dimension by factor of 4 or greater. At river outlets, however, widths generally exceed depths by a factor of at least 4 and commonly have width to depth ratios greater than 50 (Edmonds & Slingerland 2007). As a result, at river mouths, in contrast to these experiments, the relative area over which shear is generated along a bounding wall (the jet bed) exceeds the area over which free shear and turbulence is generated at the lateral margins of the jet. The turbulence structure of such bounded jets, therefore, develops due to both shear between the jet discharge and the receiving waters and from shear along the bottom wall boundary at the bed. Foss & Jones (1968) concluded, from studies on plane jets bounded on two sides by walls, that the turbulent structure of bounded jets is more complex than would be derived by the simple superposition of the turbulent structure of an unbounded plane jet with the turbulence expected from a wall influenced boundary layer flow. Experimental studies (e.g. Foss & Jones 1968; Holdeman & Foss 1975; Giger *et al.* 1991) of bounded jets indicate that the bed friction vertically alters the mean velocity structure and entrainment rates and may lead to the development of secondary circulation within portions of the jet.

Here we present the hydrodynamic results of a laboratory study aimed at determining the morphodynamic controls on the development of bounding levees along the margins of sediment-laden flows entering still waters. Our experimental setup up was designed to model flow conditions observed at the discharge of secondary channels entering floodplain lakes (e.g. tie channels of Rowland *et al.* 2005; Rowland & Dietrich 2006; Rowland *et al.* in press) (figure 1). In an attempt to model outlet conditions observed in the field, our experimental setup included a pair of 'proto-levees' which provided partial but diminishing confinement of the flow over the first 1 m of the basin. In this respect our results are not directly comparable to prior work on bounded-plane jets (e.g. Foss & Jones 1968; Holdeman & Foss 1975; Giger *et al.* 1991; Dracos *et al.* 1992); however, by a downstream distance of ~ 8 channel outlet widths our experimental jet exhibits mean properties and self-similarity consistent with prior works on plane jets, suggesting a limited effect of our unique entrance conditions on the 'far-field' properties of the jet.

A striking and characteristic feature of both our experimental and prototype flows is the presence of a large-scale quasi-two-dimensional 'meandering' turbulent structure that develops across the breadth of the jet (figure 1 and an electronic supplementary video available with online version). Similar features have been observed in prior experimental studies and in nature (e.g. Giger *et al.* 1991; Dracos *et al.* 1992; Seo & Kwon 2005). Dracos *et al.* (1992) found that these quasi-two-dimensional structures have limited effect on the mean structure and spreading of jets but do influence the mixing of fluid within the jet. Jirka (2001) argued that such large-scale two-dimensional coherent structures likely have a significant influence on the lateral momentum exchange in rivers, estuaries and coastal zones and suggested that

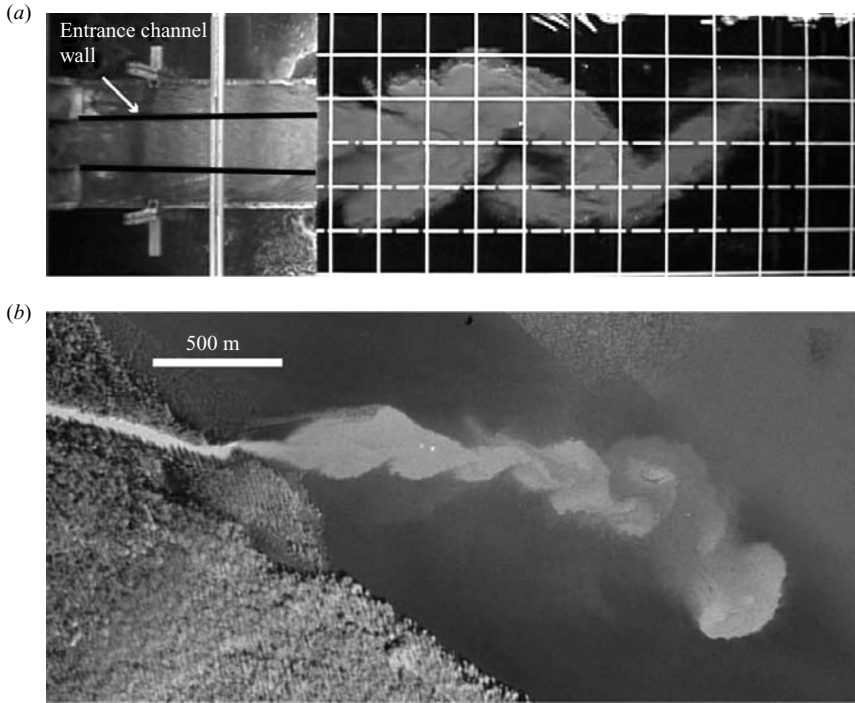


FIGURE 1. (a) Jet meander highlighted by fluorescein dye (visible as grey against the black background). Flow enters the experimental basin at the left and flows to the right. The entire field of view is $320\text{ cm} \times 120\text{ cm}$ (grid squares are $20\text{ cm} \times 20\text{ cm}$). The entrance channel occupies the first 100 cm and widens from 22 cm at the outlet to 25 cm at the gridded bed, over the same distance the height of the channel walls decrease from 4 to 0 cm . The depth of the jet is 5 cm . The dye is less visible along the channel due to the grey background. The instabilities associated with the meandering structure result in large vortices along the margin of the jet. At the margins, these vortices counter rotate in an upstream direction and entrain large masses of ambient basin waters (dark areas within the boundaries of the jet) into the core of the jet. (b) Aerial photograph of a tie channel outlet discharging into an oxbow lake (flow is from left to right) connected to the Lower Mississippi River near Baton Rouge, LA, USA. At the break in the trees the channel changes orientation from the angling to the lower to the upper right hand corner of the image. A portion of the partially submerged tree-lined levee, just below the right half of the scale bar marks the upper boundary of the channel. The ends of the subaqueous levees occur $\sim 500\text{ m}$ from the tree-lined and well-confined channel. The meandering jet remains in-line with the outlet channel for $\sim 1500\text{ m}$, though the most downstream vortex appears to be meandering off of the jet centreline. Image Source: 1998 US Geological Survey Digital Ortho-Quarter Quadrangle.

quantifying such processes is an important goal for understanding the hydrodynamics of these systems.

The purpose of this paper is threefold. First, we present a direct test of the applicability of previously determined experimental constants for the mean properties of plane jets applied to flows with aspect ratios and outlet geometries approaching that observed at river and tidal outlets. Second, we quantify the turbulent properties of a wide aspect ratio jet and explore the vertical variations in these properties with distance from the bottom bounding wall. Finally, through the use of auto-correlation and one-dimensional spectral analysis of the velocity time series, we decompose the jet turbulence into quasi-two-dimensional meander dominated turbulence and

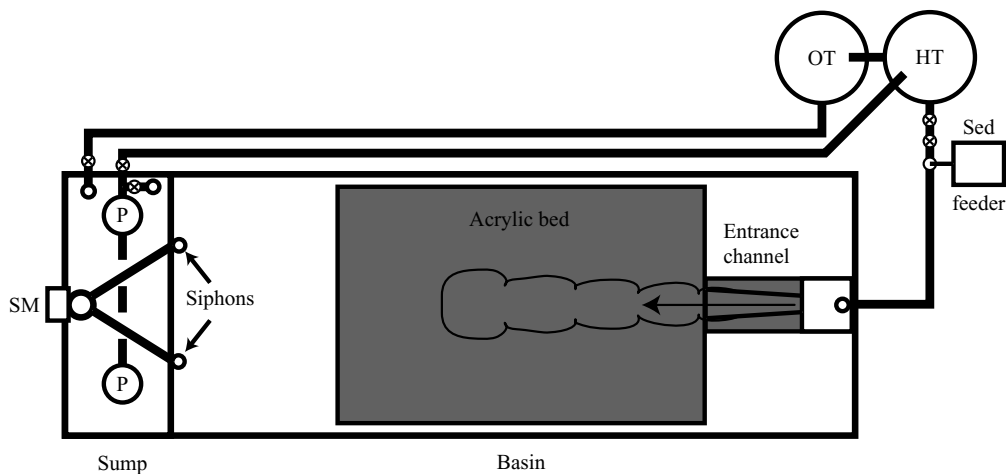


FIGURE 2. Planview of experimental flume set-up. Water is recirculated by a pair of pumps (P) from the sump to the head tank (HT) where it both feeds the flume and overflows into the overflow tank (OT). Water enters the basin on the right and is withdrawn by siphons connected to a head cylinder controlled by a stepper motor (SM). ‘Sed feeder’ marks the location of a sediment feeder used in companion experiments (Rowland 2007).

three-dimensional bed-shear dominated turbulence. Based on this analysis we quantify the influence of the large-scale coherent structures on the lateral shear and lateral transfer of momentum across the jet.

2. Experimental setup

We created an experimental plane jet by introducing a 5 cm deep flow into a basin with horizontal dimensions of $8\text{ m} \times 3\text{ m}$ (figure 2). The basin contained 45 cm of standing water with an acrylic bed positioned 5 cm below the water surface. To determine the effective roughness of the acrylic bed, Rowland (2007) used measured near bed Reynolds stresses across the jet to calculate bed shear stress (τ_b), and estimated bed friction (c_f) values assuming a quadratic friction law ($\tau_b = \rho c_f U^2$, where ρ is fluid density and U is streamwise velocity). These friction factors ranged from 0.004 to 0.0075. Flow entered the basin via a $0.54\text{ m} \times 0.50\text{ m}$ stilling box and passed through a flow straightener to exit out a 22 cm wide outlet into a 1 m long ‘channel’ and then flowed across a $2.4\text{ m wide} \times 3.7\text{ m long}$ acrylic bed supported by an aluminium frame. An average outlet velocity (U_o) of 0.53 m s^{-1} produced a fully turbulent jet with a Reynolds number of 2.7×10^4 . Water was extracted from the basin for recirculation via a pair of 7.6 cm diameter siphons located at the opposite end of the basin from the inflow and $\sim 20\text{ cm}$ below the height of the acrylic bed. The outflow through the siphons and the elevation of the water in the basin was controlled by a head cylinder mounted on a computer controlled Velmex, Inc. BiSlide[®] linear positioner.

The entrance channel only partially constrained the jet and therefore we treat the upstream end of this channel as the jet outlet. At the outlet, the 0.64 cm thick acrylic channel walls were 4 cm high (1 cm below the water surface) and decreased in elevation to 0 cm in height 1 m from the outlet where the channel merged with the larger acrylic bed. Over the same distance, the separation between channel walls increased from 22 to 25.5 cm. This entrance configuration was motivated by two experimental objectives. First, we wished to simulate outlet conditions of our prototype channels in which

the transition from full confinement to complete unconfinement typically occurs gradually as bounding levees progressively decrease in height and widen (Rowland & Dietrich 2006; Rowland 2007). Second, as part of a larger study to understand the morphodynamic development of leveed channels (e.g. Rowland 2007), we found it necessary to ease the transition to unconfinement to avoid a depositional gap in sedimentation directly at the jet outlet.

Both the channel and acrylic bed were horizontal with a maximum elevation variation of 4 mm (8 % of the average flow depth) and a standard deviation 0.6 mm across the measurement domain. During velocity profiling, the basin water level was periodically checked and siphon heights adjusted to maintain a static depth of 5.0 ± 0.1 cm over the bed. The cause of minor basin water level variations is not definitively known. Our best explanation is that, despite purging at the beginning of each measurement period, air leaked into the siphon piping; if sufficient air collects in the elbow of the siphons the effective cross-section of the pipe is reduced and the flow through the pipe decreases resulting in an increase in the basin water level. Additionally, temperature in the experimental facility could not be controlled and variations in basin water temperature over the course of a day (both from the ambient temperature and from the pumps recirculating the flow) may have contributed a minor amount to the observed change in the basin water level.

Three-dimensional velocity measurements were made using a side-looking Nortek Vectrino Acoustic Doppler Velocimeter (ADV) affixed to a point gage mounted to an aluminium frame spanning the basin. ADV measurements were recorded for a period of 120 s at an output frequency of 25 Hz. The sampling duration was chosen based on prior experiments with similar flow characteristics. In the experiments presented here, the average period of the meandering structure was 6 s or 5 % of the sampling duration; the maximum meander time scale recorded was 20 s. Precision milled slides mounted into slots in the aluminium framing allowed the ADV to be manually positioned across the jet. The point gage had a minimum increment of motion of 0.3 mm. Point velocity measurements were made in a series of vertical profiles collected at 2 cm spacing across half the jet and at 14 cm spacing down jet starting 76 cm and ending 300 cm downstream of the channel outlet. Only half the jet was profiled based on the assumption of symmetry about the centreline of the time-averaged properties of the jet. In cross-section, measurements extended from 2 cm over the midline of the bed (on which the jet was centred) to the distal – most edge of the jet for which reliable velocity measurements could be recorded given the intermittent and highly variable turbulence. An entire series of profiles was collected at each cross-section before the probe was advanced in the downstream direction. Normalized by the channel outlet width (B), measurement sections spanned a distance of x/B of 3.5–13.6, where x is the streamwise distance from the outlet. The streamwise extent of velocity measurements was constrained by the size of the instrument frame.

In each vertical profile five time series were recorded. The lowest depth interval at each profile location was 0.8 cm above the bed; this is the distance from the base of the ADV probe casing to the centre point of the acoustic transmitter. The four successive measurements were made at fixed elevations relative to an arbitrary datum. The heights of these measurements were 1.02, 1.32, 2.78 and 4.25 cm relative to the mean bed elevation. The relative elevations of the sample heights (z) to the total flow depth (H) were 0.16, 0.21, 0.26, 0.56 and 0.85. The selection of measurement elevations was dictated by the physical constraints of collecting measurements in the shallow flow. A sampling goal was to collect at least three time series per profile with all three velocity components in order to construct turbulence stress profiles. Due to

partial probe emergence from above the water surface at heights greater than 1.32 cm interval, only horizontal velocity components were recorded in the two upper most intervals ($z/H = 0.56$ and 0.85). An additional section of measurements was collected at the outlet of the flow straightener to quantify flow velocities and total discharge entering the basin.

3. Data processing and analysis

3.1. Time series filtering and processing

We processed the individual velocity files to both filter the data and analyse the mean and turbulent flow characteristics at each measurement location. To remove Doppler noise and minimize aliasing near the Nyquist frequency [f_N (half the sampling frequency)] we low-pass filtered each velocity component using the Gaussian smoothing function $w(t)$ presented in Biron, Roy & Best (1995) and Lane *et al.* (1998):

$$w(t) = (2\pi\sigma^2)^{1/2} \exp(-t^2/2\sigma^2) \quad (3.1)$$

$$\sigma = \left(\frac{\ln(0.5)^{1/2}}{-2\pi^2 f_{50}^2} \right)^{1/2}, \quad (3.2)$$

where t is time, $f_{50} = f_D/6$ and f_D is the sampling frequency. The filter eliminates variance at frequencies greater than the Nyquist frequency (Biron *et al.* 1995; Lane *et al.* 1998).

Following low-pass filtering, the data were further filtered by removing all velocity measurements with signal correlation values less than 70%. Finally, each velocity component (x , y , z) was divided into windows consisting of 1000 measurements ($\sim 1/3$ each time series) and all points that exceeded the windowed mean by more than three standard deviations were removed as spikes not representative of the overall time series. Spike removal on subwindows was required because low-frequency large-amplitude variations in velocity resulted in large standard deviations across the entire time series and spikes could not be reliably excluded from the complete time series without removing coherent portions of the signal.

An average of 96% of all velocity measurements were retained for analysis following filtering. The majority of data screened out due to low signal correlations or spikes occurred in the highly intermittent low-velocity margins of the jet. Across the core of the jet, an average of 98% of the data were retained for analysis. Under a prior experimental run that differed in set-up from the present study only in the presence of a sloped bed and slightly lower initial discharge, 10 duplicate vertical profiles were measured. The profile measurements were conducted on different days following shut down and restart of the system and repositioning of the ADV probe. At 31 measurement locations, ranging from two to four duplicate time series per location, the coefficient of variation in the mean streamwise velocity ranged from 0.1% to 7% with an average of 3%.

Due to minor temporal variations in basin water level (see §2) over the course of, or between, measurement days, and local variations in bed elevation (see §2), the relative error between measurement points is likely to be the greatest in the downstream direction. Despite this source of error, the difference between the measured centreline velocity profiles and that of an ideal jet, as expressed by the best fit velocity decay equations, was relatively small. The residuals from the best fit equations for centreline velocity averaged 1.1% of the measured velocity and the maximum residual in all measurement layers was 4.8% of the measured velocity. For the depth-weighted mean

centreline profile these values were 0.65 % and 1.2 %, respectively. All measurements in individual vertical profiles were conducted over an approximately 15 min interval. All measurements at an individual cross-section were typically collected over the course of a single day.

Three aspects of the flume set-up required a post-data collection transformation to align all of velocity vectors to a common reference frame. First, the ADV probe head was mounted on a flexible cable that was mounted onto a point gage affixed to the instrument frame spanning the basin. Due to this configuration, probe orientation precisely perpendicular to the bed and parallel to the jet centreline could not be achieved. Second, midway through profiling of the jet, other experimental demands on the equipment required that the ADV probe be removed and reinstalled. Finally, every effort was made to align the centre of the jet with the centreline of the basin, however, given the width of the jet, precise alignment of the jet and the flume centreline could not be assured. The three orthogonal velocity components recorded by the ADV probe were rotated into a reference frame that achieved a zero mean cross-stream velocity for the time series collected along the assumed basin centreline at a relative depth (z/H) of 0.56. The highest streamwise velocity on each measurement cross-section, at distances $x/B > 8.5$, occurred at this depth interval and therefore we assume it to represent the core of the jet. The cross-stream distributions of streamwise velocities at each downstream cross-section indicate no systematic deviation in the maximum streamwise velocity from the selected centreline, suggesting limited misalignment of the jet centreline with the basin centreline. At most sections the maximum velocity occurs within one measurement interval (2 cm) of the presumed jet centreline, and at sections where the maximum velocity falls off the centreline, the velocity difference with the centreline value is within the range of measurement errors. The vertical velocity vectors were rotated to achieve a zero mean vertical velocity for all measurements recorded in the bottom three measurement intervals (no vertical velocities were recorded in two upper most layers).

3.2. Decomposition of meander-influenced turbulence

In frequency versus power space the large-scale meandering structure displays a distinct spectral signature (figure 3a). One-dimensional plots of the velocity power spectrum exhibit a characteristic -3 slope across frequencies in which the quasi-two-dimensional meander dominates the turbulent structure (figure 3a). The meander also shows a characteristic quasi-periodicity in the plots of the autocorrelation coefficient of the cross-stream velocity component (figure 3b). Similar spectral and autocorrelation characteristics were reported by Giger *et al.* (1991) and Dracos *et al.* (1992) across portions of experimental jets exhibiting the similar meandering behaviour. The frequency break between the spectra with -3 slope of quasi-two-dimensional turbulence and the $-5/3$ slope arising from three-dimensional bed-driven turbulence marks the division in time scales over which each process should dominate. While easily discernable by visual inspection of the one-dimensional spectral plots, we failed to find an automated analysis routine of the spectra to accurately identify the -3 to $-5/3$ slope transition (with more than 1500 individual time series visual analysis of each was not a feasible option). By analysing the normalized autocorrelation coefficient of the cross-stream velocity vector, however, we developed a robust method for determining the respective time scales for the quasi-two- and three-dimensional turbulence.

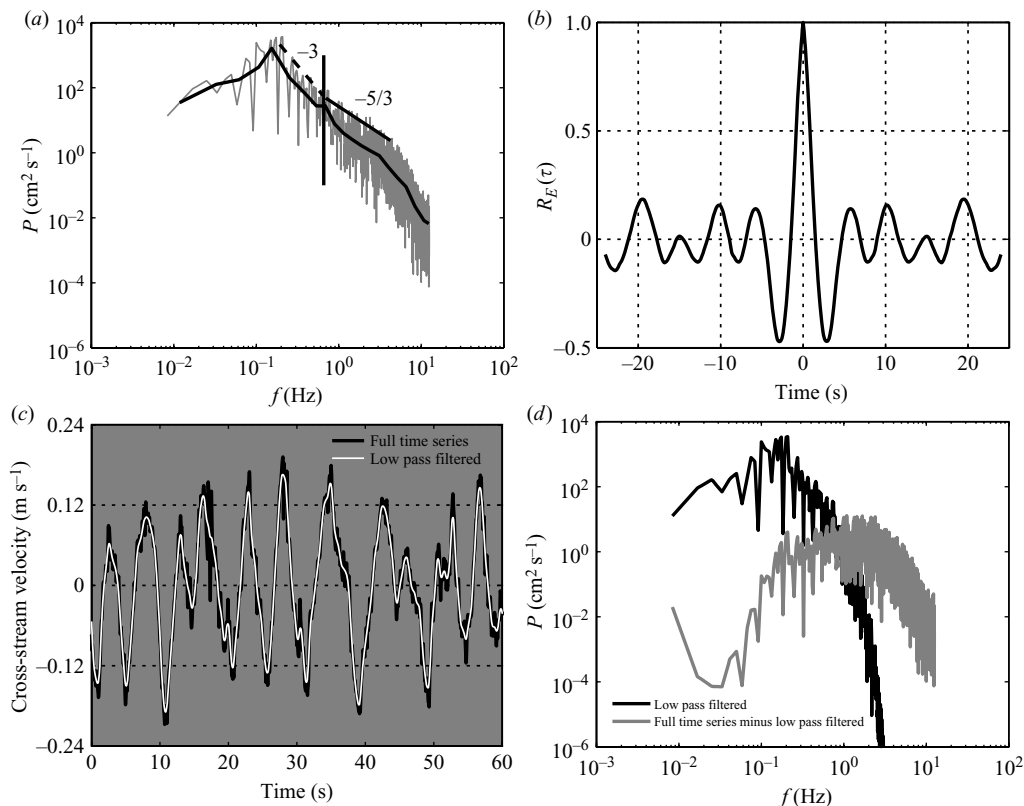


FIGURE 3. Example spectra (*a* and *d*), autocorrelation (*b*) and time series (*c*) plots of the cross-stream velocity component measured 244 cm from the outlet, 4 cm from the jet centreline and at a relative depth (z/H) of 0.85. (*a*) The complete power spectra in grey and a smoothed spectra in black. Lines labelled -3 and $-5/3$ are shown to highlight changes in the slope of the spectral power decay. The solid vertical line corresponds to the frequency at which the first zero crossing occurs on (*b*) the normalized autocorrelation time coefficient ($R_E(\tau)$); (*c*) the full time series and the time series low-pass filtered at the frequency of the first zero crossing in (*b*) to isolate the meander-generated turbulence; (*d*) power spectra for both the low-pass filtered meander time series and the time series with the meander removed.

Due to the quasi-periodicity of the meandering structure, the correlation and anti-correlation of a velocity time series measured at a fixed location as the meander passes that location also shows a distinct periodicity (figure 3*b*). The first zero crossing in the normalized autocorrelation time coefficient represents $\sim 1/4$ of a full meander wavelength. Visual inspection of approximately 20% of the time series, from across the jet, indicated that the frequency associated with this first zero crossing provides an accurate estimator for the transition from quasi-two-dimensional meander-dominated turbulence to three-dimensional bed-generated turbulence.

We performed autocorrelation analysis on each velocity time series and determined the time scale associated with the first zero crossing of the cross-stream velocity vector. By setting f_{50} in (3.2) equal to this frequency, we low-pass filtered each time series to remove the high-frequency bed-generated turbulence and isolate the meander-generated turbulence (figure 3*c*). We then subtracted this filtered time series from the full time series. The remaining or residual (high-frequency bed-generated) turbulence was then analysed. The difference between the residual turbulence and the

Depth interval (z/H)	Decay constant	C_u	ζ_u	$db/dx(C_b)$	ζ_b
0.16	-0.56	0.25	2.30	0.096	-0.96
0.21	-0.53	0.20	0.50	0.088	-1.94
0.26	-0.58	0.22	1.68	0.105	0.104
0.56	-0.49	0.19	0.78	0.096	-0.94
0.85	-0.52	0.19	0.32	0.109	0.57
Depth-weighted mean	-0.53	0.20	0.97	0.103	-0.13

TABLE 1.

full time series represents the influence of the meander on the jet. Figure 3(d) shows the result of this turbulence decomposition in power versus frequency space.

4. Experimental results

Following established jet terminology, we divide our experimental jet into two distinct regions: a zone of flow establishment (ZOFE) and a zone of established flow (ZOEF). The transition from the ZOFE to the ZOEF marks the downstream location at which turbulence generated by shearing along the margins of the jet effects the entire jet (Bates 1953). In the ZOFE of the centreline of the jet remains unaffected by marginal shear and its velocity is maintained at the outlet velocity. Across the ZOEF, the centreline velocity will decay at a characteristic rate for the given jet geometry. The transition between ZOFE and ZOEF is typically reported as occurring between 4 and 6 outlet widths downstream of the outlet (Albertson *et al.* 1950; Tennekes & Lumley 1972). Bates (1953) observed, however, in reference to river mouths, that a third ‘transitional’ zone may occur between the ZOFE and ZOEF extending to a distance of eight channel widths. In this ‘transitional’ zone the centreline velocity decreases but at a lesser rate than that observed in the ZOEF. A self-preserving condition should develop in the ZOEF allowing the application of empirically derived similarity solutions for the mean jet structure.

Based on the mean structure and turbulent characteristics, the transition to a ZOEF appears to occur between eight and nine channel widths downstream of the outlet in our experiments. Due to possible influences from our unique outlet conditions and the absence of self-similarity in our ZOFE, results from this region are not directly comparable to prior plane jet studies. As such, in the following sections we present data for the entire flow field but focus primarily on observations from the ZOEF.

4.1. Mean velocity structure

4.1.1. Streamwise velocity

At distances $x/B > 8.5$ the streamwise velocity on the centreline of the jet (U_m) normalized by the outlet velocity (U_m/U_o) decreased at an $\sim x^{-1/2}$ rate (4.1) consistent with well-established theory and data for plane jets (Schlichting 1968; Tennekes & Lumley 1972). The velocity decay rate ranged from a maximum of -0.58 in the $z/H = 0.26$ layer to a minimum of -0.49 in the $z/H = 0.56$ layer with a depth-weighted mean value of -0.53 (table 1).

$$\frac{U_m}{U_o} = \left(\frac{x}{B}\right)^{-1/2}, \quad (4.1)$$

For comparison to prior studies on wall-bounded plane jets (e.g. Giger *et al.* 1991; Dracos *et al.* 1992), the squared ratio of the outlet velocity to the centreline velocity

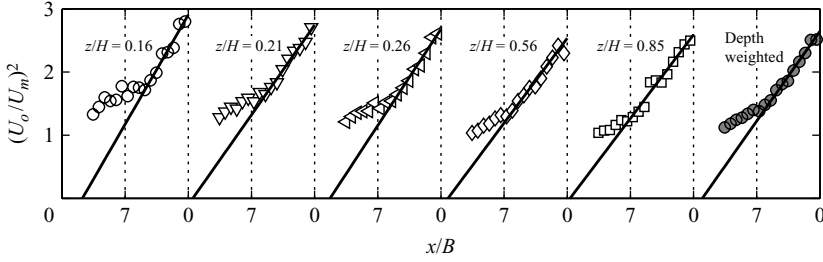


FIGURE 4. Square of the ratio of the outlet velocity to the centreline velocity versus normalized distance down jet. Individual measurement layers shown by relative depth. Solid line represents best fit of (4.2) to velocities in the ZOEF.

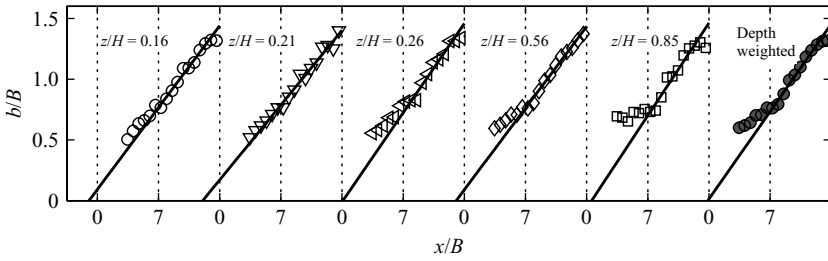


FIGURE 5. Plot of normalized velocity half-widths ($b(x)/B$) versus relative distance down jet from the channel outlet. Solid lines are best fit of (4.3) for half-widths across the ZOEF.

$((U_o/U_m)^2)$ is plotted by measurement layer in figure 4. In a self-similar jet, this ratio of velocities should display a linear dependence on distance from the jet outlet (Dracos *et al.* 1992)

$$\left(\frac{U_o}{U_m}\right)^2 = C_u (\zeta - \zeta_u), \tag{4.2}$$

where C_u is a kinematic ‘spreading’ parameter (Giger *et al.* 1991) (the slope of the straight lines in figure 4), $\zeta = x/B$ and ζ_u is the virtual origin. We fit (4.2) to the centreline velocity ratios measured across the ZOEF for each measurement layer and the best fitting values for C_u and ζ_u are presented in table 1. Values of C_u ranged from 0.19 in the uppermost near-surface layer to 0.25 in the lowermost near-bed layer with a depth-weighted mean value of 0.20. Giger *et al.* (1991) reported a range of C_u values of 0.182 (for their widest ($B/H = 0.25$) jet) to 0.205. The average C_u value from the compilation of 49 prior studies of plane jets by Giger *et al.* (1991) is 0.17.

Figure 5 graphically depicts the lateral expansion of the jet, measured by the velocity half-width ($b(x)$), with distance from the outlet. The velocity half-width represents the lateral distance (y) from the jet centreline, at any distance x from the outlet, where the local streamwise velocity (U) is half that of the jet centreline (U_m). We estimated the values of $b(x)$ shown in figure 5 by linearly interpolating between measurement points. In a self-similar jet, the half-width increases linearly with distance from the outlet (Abramovich 1963; Tennekes & Lumley 1972). This relationship was expressed by Giger *et al.* (1991) and Dracos *et al.* (1992) in the following form:

$$\frac{b}{B} = C_b (\zeta - \zeta_b), \tag{4.3}$$

where $C_b = db/dx$, and ζ_b is the virtual origin. Layer specific and the depth-weighted mean values for the C_b and ζ_b for the ZOEF are presented in table 1. In experiments detailed by Giger *et al.* (1991) and Dracos *et al.* (1992) C_b ranged from 0.96 to 0.106 and Giger *et al.* (1991) report an average spreading rate of 0.106 for 49 experiments on plane jets.

At distances $x/B < 7$, values of b/B show greater deviation from the straight line defined by (4.3) with proximity to the upper free surface. This deviation reflects an ~ 1 mm elevation of the free water surface at the outlet and along the upper portion of the outlet channel. Bates (1953) observed that at river mouths similar surface potentials should exist and that in this respect rivers systems would deviate from pure jets in which the flow is driven solely by inertial forces.

Under conditions of self-similarity, the cross-stream distribution of streamwise velocity at any section of a jet approximates a normal distribution (Tollmien 1926; Reichardt 1942; Albertson *et al.* 1950; Abramovich 1963; Schlichting 1968) such as the one proposed by Reichardt (1942) and used by Giger *et al.* (1991) to describe their experimental jets

$$\frac{U(y)}{U_m} = \exp(-\ln(2)\eta^2), \quad (4.4)$$

where $U(y)$ is the velocity at any lateral location, and $\eta = y/b(x)$. Figure 6 presents the normalized lateral velocity distributions for the depth-weighted mean velocities and velocities measured at depths of $z/H = 0.16$ and $z/H = 0.85$. At distances $x/B > 5.4$ all profiles exhibit a normal distribution of streamwise velocity. Near the jet outlet ($x/B \leq 5.4$) velocities at locations $\eta < 1$ are elevated relative to the predicted normal distribution. Despite the varying height of the entrance channel walls bounding the jet in the range $0 < x/B < 4.5$, we observe no clear differences in the normalized structure of the lateral velocity distribution between the five depth intervals measured out to $x/B = 6$. Since the uppermost measurement layer ($z/H = 0.85$) is unbounded for the length of the entrance channel, the agreement in profile structure between this layer and the near-bed layer ($z/H = 0.16$), which does not exceed the height of the channel walls until $x/B = 3.6$, suggests that the presence of the channel walls have a limited influence on the distance to the onset of velocity self-similarity. Additionally, the location at which we observe the commencement of self-similarity to occur coincides with that reported for prior experimental work on plane jets (Tennekes & Lumley 1972).

Vertical profiles of streamwise velocity along the centreline of the jet (figure 7) display three distinct changes between the ZOFE and ZOEF. First, across the ZOFE ($x/B < 8.5$) the bottom boundary layer, as evidenced by logarithmic velocity distributions (solid lines in figure 7), extends across the full depth of the flow. After the transition to the ZOEF at $x/B = 8.5$ logarithmic profiles may only be fit to the lower quarter to half of the flow. Second, the vertical gradient in velocity decreases abruptly from the ZOFE to the ZOEF. Across the ZOFE the near-bed velocities range from 10% to 20% less than the near surface. In the ZOEF, however, the near bed to near surface difference ranges from 0% to 8%. Finally, associated with this flattening of the velocity gradient is a shift in the velocity maximum from the near-surface measurement layer to the layer close to the mid depth ($z/H = 0.56$). The difference in velocity between the two measurement layers is small, ranging from 0.4% to 6% and averaging 2.6% (in the order of the measurement errors), but consistent across the ZOEF.

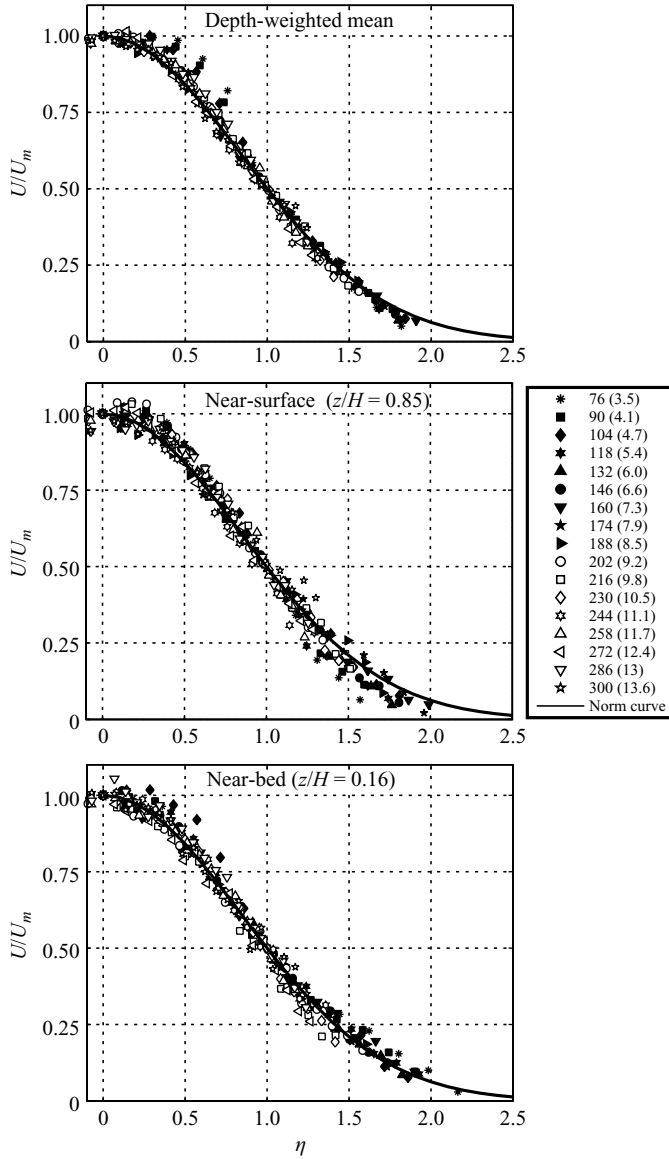


FIGURE 6. Plot of the normalized depth-weighted mean, the near-surface and the near-bed streamwise velocities by the normalized cross-stream coordinate (η). The centre of the jet lies at $\eta=0$. Solid symbols correspond to measurement cross-sections within the ZOFE and open symbols correspond to sections measured in the ZOEF. The solid line represents a similarity profile defined by (4.4). Numbers in the legend represent distance in centimetres from the outlet and the normalized distances (x/B) are in parentheses.

4.1.2. *Cross-stream velocity*

In a self-similar plane jet the lateral distribution of cross-stream velocities (V) should be approximated by the following relationship (Bradbury 1965):

$$\frac{V}{U_m} = \frac{db}{dx} \left(\eta f - \frac{1}{2} \int_0^\eta f d\eta \right), \tag{4.5}$$

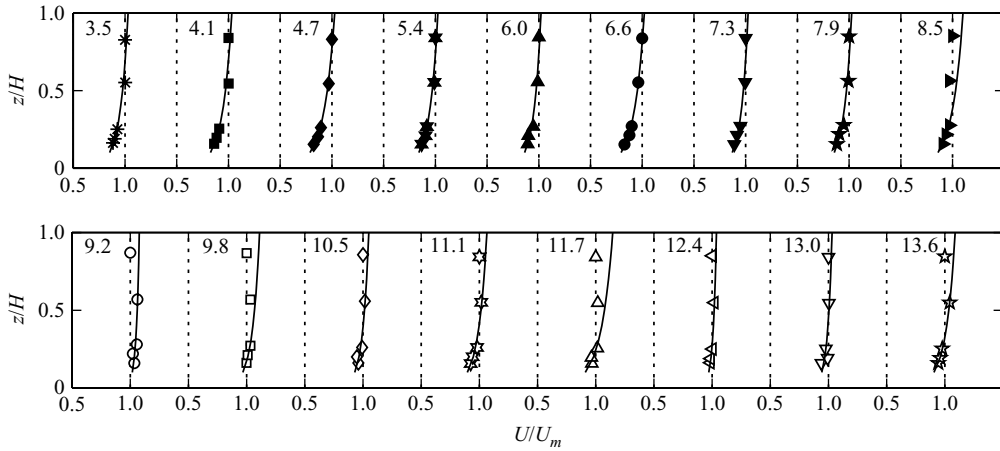


FIGURE 7. Vertical profiles of streamwise velocity along the centreline. Numbers at the upper left of each profile indicate normalized distance (x/B) from the outlet (flow direction is left to right, top to bottom across the figure). In each profile the velocities are normalized by the streamwise velocity in the near-surface measurement ($z/H = 0.85$) layer. Solid lines are the best fit logarithmic velocity profiles for each location.

where f is the function defining the normal distribution of mean streamwise velocities and db/dx represents the spreading rate of the velocity half-width. Plots of the depth-weighted mean, the near-surface and near-bed cross-stream velocities are shown in figure 8. Also shown are the predicted self-similar distributions ((4.5) based on f equal to the right-hand side of (4.4) and the values of db/dx presented in table 1). The near-surface cross-stream velocity distribution (figure 8*b*) shows good agreement with (4.5) across both the ZOFE and ZOEF. The negative deviation of depth-weighted mean distribution (figure 8*a*) from (4.5) reflects the influence of an increase in the relative strength of the outward directed velocities near the mid depth measurement layer (not shown). Figure 8(*c*) shows an increase in the overall scatter in the ZOFE cross-stream velocities with proximity to the bed. In the near-bed layer of the ZOEF, the greatest deviations in cross-stream velocity distributions from (4.5) occur near the centre of the jet ($\eta < 0.5$).

A complete cross-section (all measurement depths), from the centreline ($\eta = 0$) to the jet margin, of cross-stream velocities at $x/B = 8$ is presented in figure 9. Near the margin of the jet there is a strong vertical gradient in cross-stream velocities with small outward directed velocities occurring near the bed and strong inward velocities near the surface of the jet.

4.2. Turbulence intensities

The velocity normalized turbulent intensities, as expressed by the root mean square of the velocity (r.m.s. (u') and r.m.s. (v')), increase in magnitude with distance from the jet outlet along the centreline of the jet (figure 10). Near the distal end of the measurements ($x/B > 12$), r.m.s. (u')/ U_m appears to achieve the expected ratio of ~ 0.22 for self-preserving plane jets (Tennekes & Lumley 1972; Giger *et al.* 1991; Dracos *et al.* 1992; Jirka 1994). In plane jet studies reported in Bradbury (1965), constant relative turbulence intensities were not observed until distances of $x/B > 20$, and for the widest jet reported in Dracos *et al.* (1992) relative intensities continued to increase out to distance of $x/B = 150$. On the centreline, cross-stream turbulence intensities begin to exceed streamwise intensities at distances $x/B > 6$. The maximum

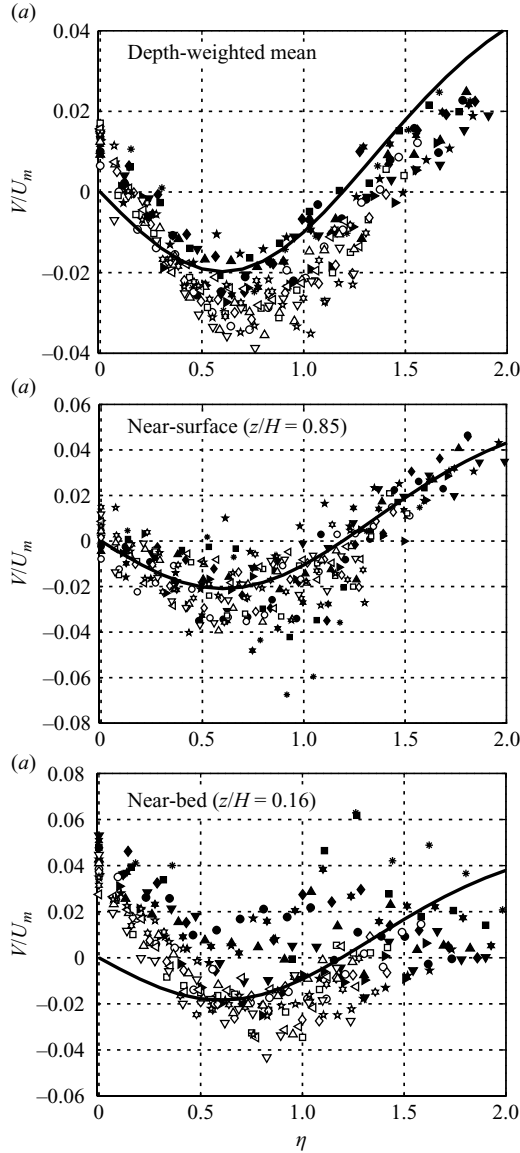


FIGURE 8. Normalized plots of cross-stream velocity for the depth-weighted mean, near-surface ($z/H = 0.85$) and near-bed ($z/H = 0.16$) measurement layers. Negative values indicate outward flow towards the jet margins and positive values reflect inward flow. Solid lines represent (4.5) for each layer. Symbols are same as in figure 6 – solid symbols correspond to sections $x/B < 9$ and open symbols correspond to sections $x/B > 9$.

streamwise intensities which occur at $\sim \eta = 0.75$, however, are of equal magnitude as the centreline cross-stream intensities (figure 11). Both $\text{r.m.s.}(u')$ and $\text{r.m.s.}(v')$ exhibit a step increase at $x/B = 8.5$ coincident with the onset of the ZOEf.

In contrast to the distributions of cross-stream velocities, turbulent intensities show limited variation in magnitude or distributions from the bed to the surface across the ZOEf (figure 11). The cross-jet distributions of $\text{r.m.s.}(u')/U_m$ and $\text{r.m.s.}(v')/U_m$ both show a jump in turbulence intensities at distances of $x/B > 8.5$ (figure 11), though the

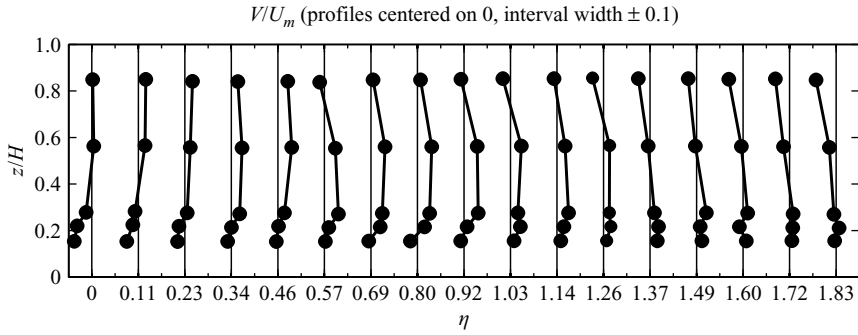


FIGURE 9. Vertical profiles of cross-stream velocity on a cross-section located at $x/B = 8$. Profiles are evenly spaced at 2 cm intervals from the jet centreline ($\eta = 0$) to the jet margin, labels on the bottom axis reflect the cross-stream distance from the centreline normalized by the depth-weighted mean velocity half-width. Each profile is centred on a normalized velocity of zero. Points located to the right of each profile line reflect outward flow towards the margin of the jet. Points on the left reflect inward flow. The distance in V/U_m between profiles is 0.10.

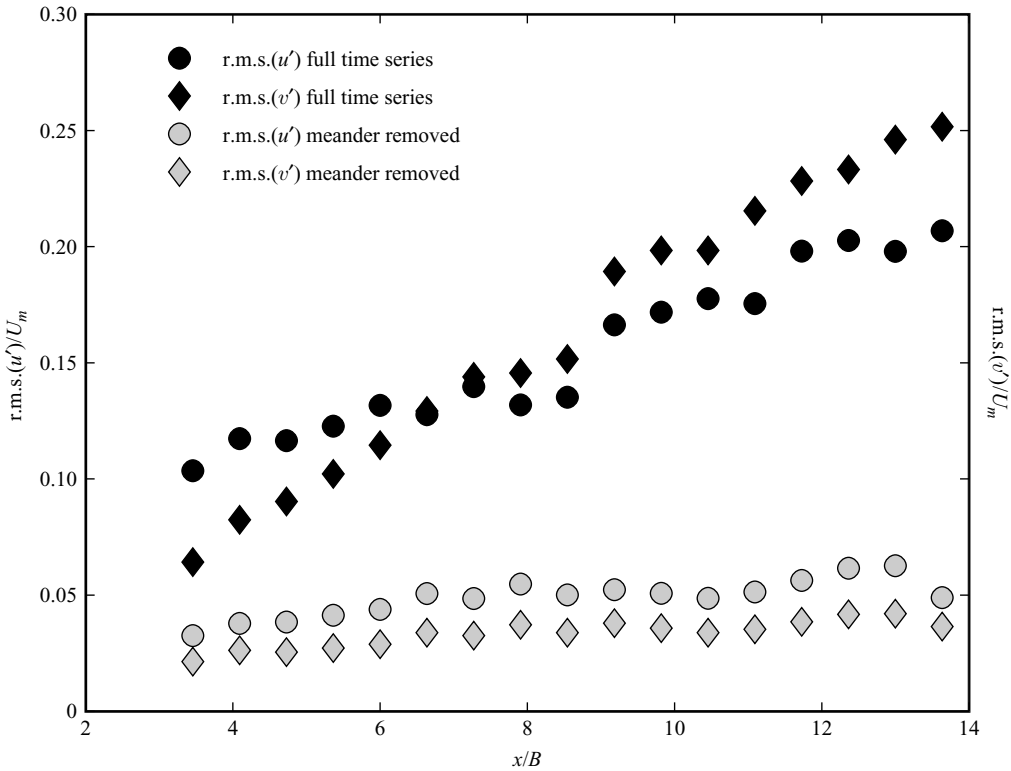


FIGURE 10. Plots of the depth-weighted mean centreline $r.m.s.(u')$ and $r.m.s.(v')$ normalized by the mean centreline streamwise velocity (U_m) for both the full time series and with the lower-frequency turbulence removed.

distribution of $r.m.s.(u')/U_m$ exhibit similar patterns from the ZOFE to ZOEF. The $r.m.s.(v')/U_m$ values, in contrast, show an inward propagation of increasing intensity within the range $3.5 < x/B < 9$ which highlights the increasing influence of the lateral

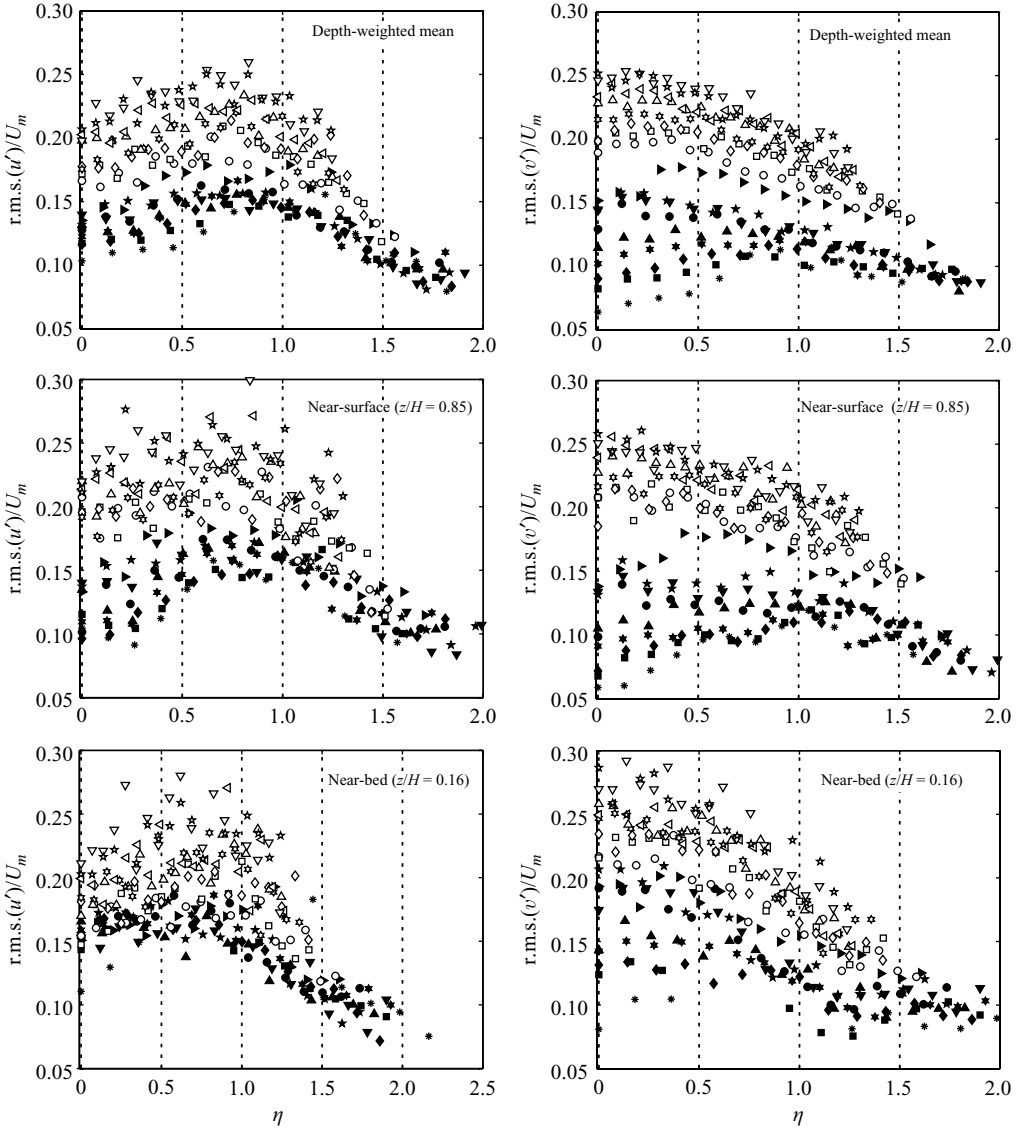


FIGURE 11. Plots of ratios of velocity r.m.s. to centreline streamwise velocity for both streamwise and cross-stream velocity vectors calculated for the entire velocity time series and averaged on a depth-weighted basis and shown for the near-surface and near-bed layers. Data are plotted by measurement cross-sections downflume and the lateral position (η) of each measurement is normalized by the local (cross-section) velocity half-width. Symbols are same as in figure 6 – solid symbols correspond to sections $x/B < 9$ and open symbols correspond to sections $x/B > 9$.

shear on the jet. At distances greater than $x/B > 9$ this shear influences the entire jet (ZOEJ) and maximum cross-stream intensities occur near the jet centreline.

Figure 10 also presents the depth-weighted mean values of $\text{r.m.s.}(u')/U_m$ and $\text{r.m.s.}(v')/U_m$ for the velocity time series with the low-frequency meander-dominated turbulence removed on the centreline of the jet. A comparison of figures 11 and 12 shows the dominant influence the large-scale meander has on the overall turbulent

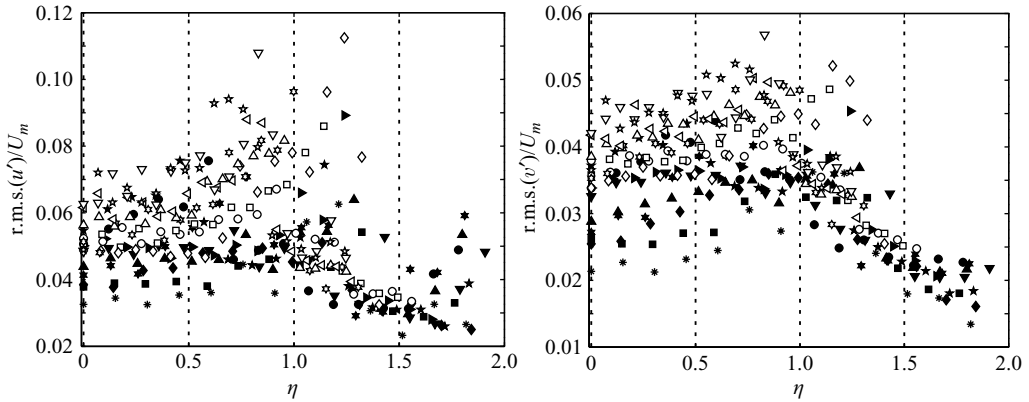


FIGURE 12. Depth-weighted velocity normalized r.m.s. values for streamwise and cross-stream velocities with the low-pass filtered meander removed from the time series to isolate the contribution of the higher-frequency turbulence. Note the different vertical scales between plots, on average $\text{r.m.s.}(u')/U_m$ values are 1.5 times greater than the $\text{r.m.s.}(v')/U_m$ values. Symbols are same as in figure 6 – solid symbols correspond to sections $x/B < 9$ and open symbols correspond to sections $x/B > 9$.

structure across the whole jet. The intensities of the higher-frequency turbulence alone ('meander removed'—figure 10) show limited growth with streamwise distance and maintain relatively constant values ($\text{r.m.s.}(u')/U_m \simeq 0.052$ and $\text{r.m.s.}(v')/U_m \simeq 0.035$) at distances of $x/B > 8$. The intensities of $\text{r.m.s.}(u')$ and $\text{r.m.s.}(v')$ are approximately 0.3 and 0.2 times the magnitudes observed in the full time series, respectively. In contrast to the relatively equal streamwise and cross-stream r.m.s. magnitudes in the full time series, at higher frequencies the streamwise intensities exceed cross-stream intensities by a factor of 1.5 on average.

4.3. Lateral shear stress

In a self-preserving jet, the magnitude of the lateral shear stress ($\tau_{uv} = -\rho \overline{u'v'}$, presented in the following sections as $(-\overline{u'v'})$, without the fluid density (ρ), for notational simplicity) should achieve a constant value relative to the mean-velocity squared (U_m^2) and have a lateral distribution characterized by (4.6) (Bradbury 1965; Tennekes & Lumley 1972)

$$-\frac{\overline{u'v'}}{U_m^2} = -g(\eta), \quad (4.6)$$

where, following Bradbury (1965),

$$-g(\eta) = -\frac{1}{2} \frac{db}{dx} f \int f d\eta. \quad (4.7)$$

Figure 13 presents distributions of $-\overline{u'v'}/U_m^2$ observed in our experiments for the depth-weighted mean, $z/H = 0.85$ and $z/H = 0.16$ conditions. Figure 13 also shows the predicted self-preserving distribution of lateral shear stress (4.6) using the right-hand side of (4.4) for f and the values of db/dx presented in table 1.

Within each vertical layer of the jet, the distributions of lateral shear stress show similar cross-stream distributions at successive downstream cross-sections. Vertically, however, the distributions of normalized lateral shear stress become less peaked and more negative from the near-surface ($z/H = 0.85$) to near-bed ($z/H = 0.16$) layers. With the exception of the most distal sections in the near-surface layer, the U_m^2

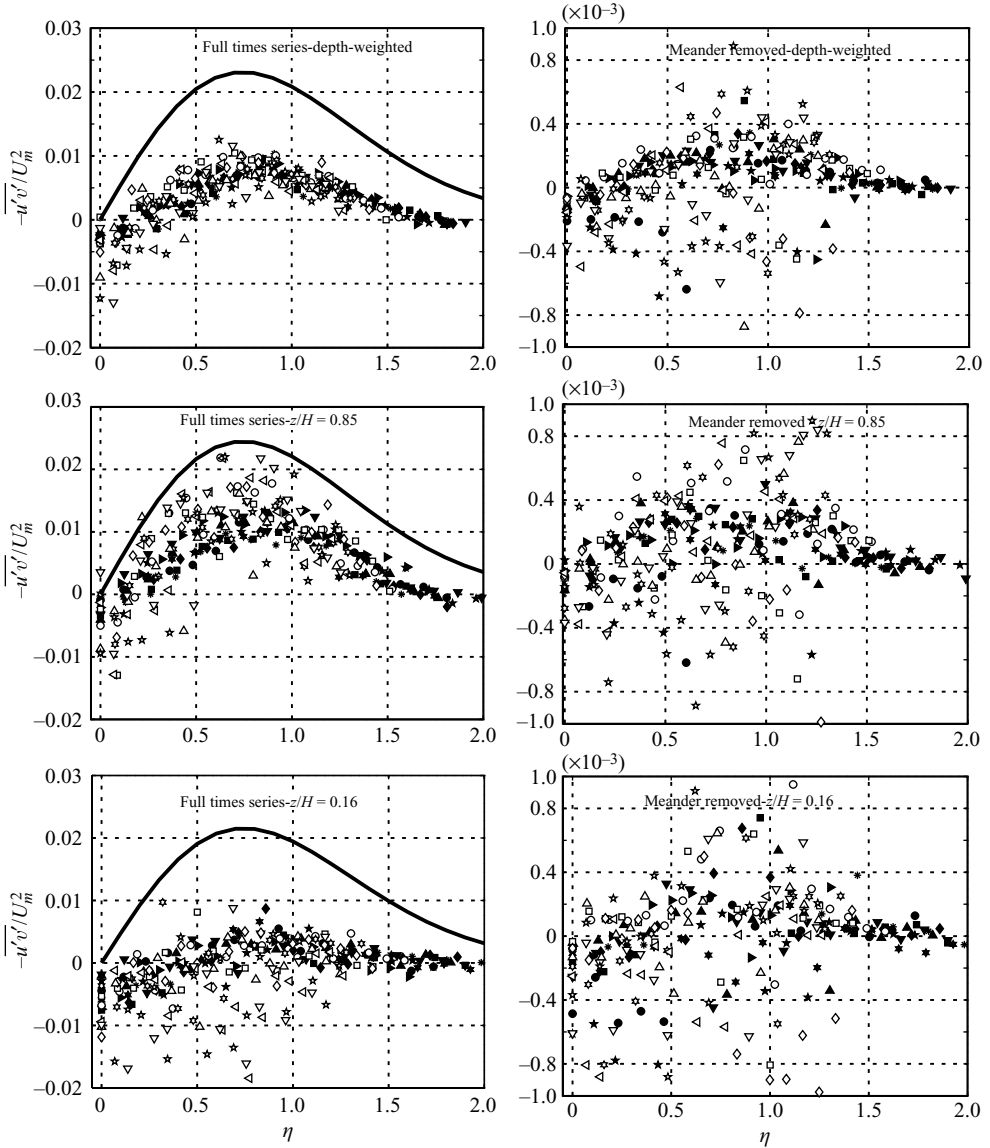


FIGURE 13. Normalized plots of $-\overline{u'v'}$ for the depth-weighted mean, near-surface ($z/H = 0.85$) and near-bed ($z/H = 0.16$) measurement layers for both the full time series and for the time series with the meander-dominated turbulence removed. The solid line is the predicted self-preserving distribution of lateral shear stress based on (4.6). Symbols are same as in figure 6 – solid symbols correspond to sections $x/B < 9$ and open symbols correspond to sections $x/B > 9$.

normalized magnitudes of lateral shear stress are reduced relative to the predicted self-preserving conditions (4.6). The deviation from self-preservation increases with proximity to the bed of the jet. Positive values of $-\overline{u'v'}/U_m^2$ are 14 times greater in the near-surface layer than in the near-bed layer on average.

Lateral shear stress estimates calculated from the time series with low-frequency turbulence removed exhibit less significant vertical variations than does the full time

series (figure 13). The average positive values of lateral shear stresses in the near-surface layer are 60 times greater in the full time series than the values from the time series with the meander-influence turbulence removed. The near-bed lateral shear stresses differ by a factor of 10 between the full and high-frequency time series.

4.4. Lateral momentum diffusivity

Turbulence drives the transfer of momentum across the jet and in a time-averaged sense this turbulent transfer of momentum may be treated analogously to a diffusive process. The condition of self-preserving turbulence and self-similar velocity distributions in jets requires that the eddy viscosity or momentum diffusivity remain constant over any lateral section of the flow (Townsend 1976). Using Prandtl's eddy viscosity hypothesis we estimate the eddy viscosity or momentum diffusivity (κ_y) of the flow using the $-\overline{u'v'}$ component of the Reynolds stress tensor and the lateral gradient in the mean streamwise velocity field

$$\tau_{uv} = \rho\kappa_y (\partial U/\partial y). \quad (4.8)$$

Over most of the length of the jet, momentum diffusivity shows a lateral variation in magnitude (figure 14). The pattern exhibits a clear dependence on the distribution of lateral shear stress (figure 13) with increasing scatter near the jet centreline as the gradient in streamwise velocity becomes vanishingly small. Excluding this centreline scatter, lateral diffusivities show a decrease in magnitude with proximity to the jet margin. This lateral decrease in momentum diffusivity accounts for the more rapid decrease in mean velocities near the margin of the jet than is predicted by the similarity function ((4.4) and figure 6) (Townsend 1976). Despite the general scatter, the near-surface ($z/H=0.85$) values of the full times series are in general agreement with maximum normalized eddy viscosities predicted by integral solutions of Agrawal & Prasad (2003) for plane jets (~ 0.023).

Similar to $-\overline{u'v'}$, the magnitude of diffusivities decreases with proximity to the bed, the depth-weighted mean values (figure 14) fall approximately midway between the near-bed and near-surface values. Across the ZOEF, momentum diffusivities decrease by a factor of 20 between the near-surface and near-bed measurement layers (figure 14).

Estimates of the diffusivity with the low-frequency meander removed from the turbulence data required both decomposition of the time series (§3.2) and correcting $\partial U/\partial y$ to account for locally higher velocity gradients at shorter time scales. This correction is required to account for the fact that while the width of the meandering structure is less than that of the entire jet (figure 1), the velocities in core of the meander are higher than the surrounding non-meandering portions of the jet. Over the measurement time interval of the full time series, the meander passes back and forth across the entire jet multiple times and the velocity gradient is proportional to the average jet velocity (U_{av}) divided by the length scale of the jet (L_j). At short time scales, the lateral gradient in streamwise velocity should be proportionally greater than the time-averaged gradient. Because we collected all of the velocity measurements in a point by point manner we have no direct measurements of lateral gradients at time scales comparable to the time scales analysed in the meander removed time series. To adjust for this, we estimate a proportionality factor (R) based on the assumption that the average discharge in the jet represents the combined discharges of the meander-dominated and non-meander-dominated portions of the jet

$$U_{av}L_j = U_\lambda L_\lambda + U_\beta(L_j - L_\lambda), \quad (4.9)$$

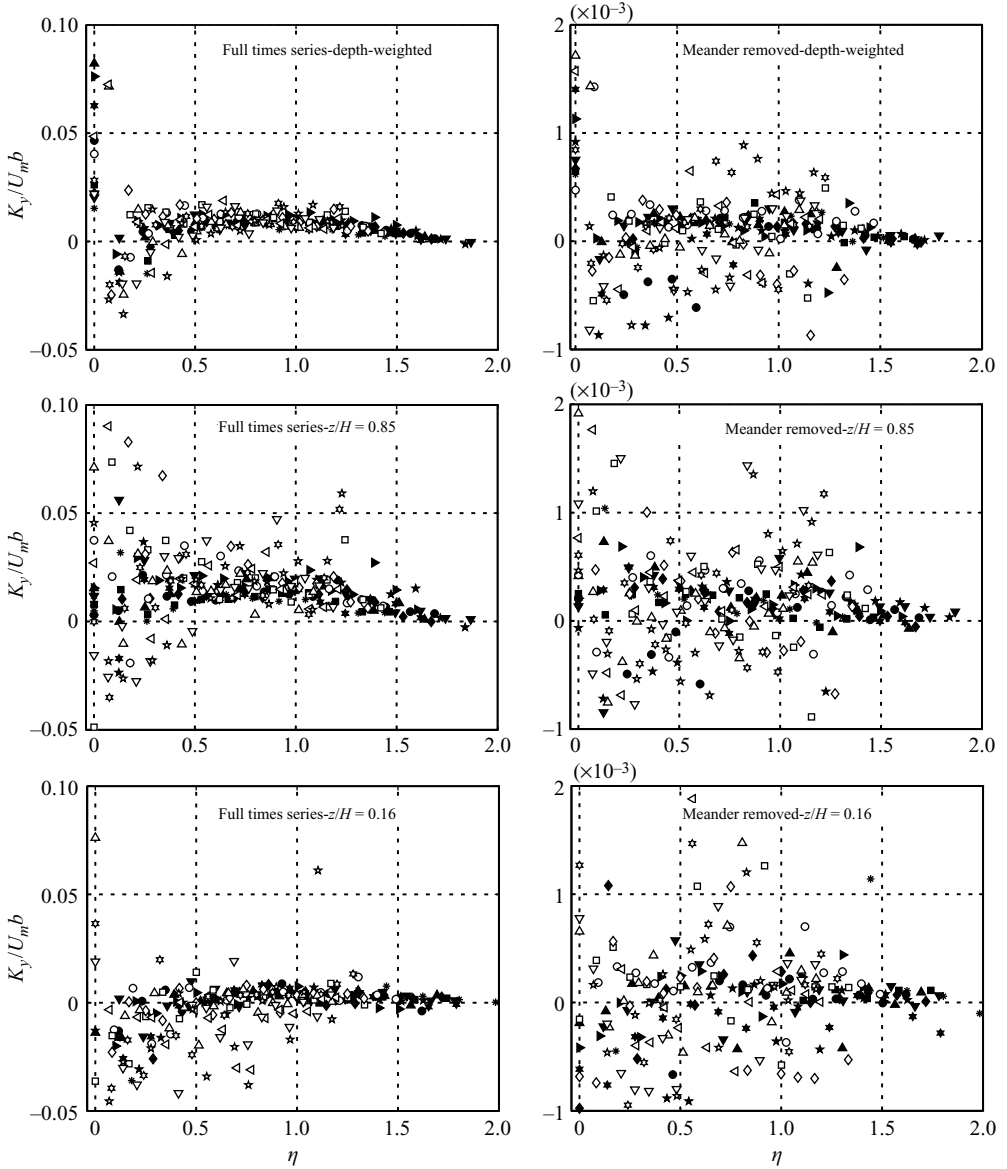


FIGURE 14. Plots of the normalized lateral diffusivity of momentum versus the normalized lateral location (η) for both the full and meander removed time series for the depth-weighted mean, near-surface ($z/H = 0.85$) and near-bed ($z/H = 0.16$) measurement layers. Symbols are same as in figure 6. Solid symbols correspond to sections $x/B < 9$ and open symbols correspond to sections $x/B > 9$.

where U_λ is the velocity in the meandering portion of the jet which has a length scale L_λ and that the remaining portion of the jet has a velocity of U_β . R then relates the time-averaged velocity gradient to the short time scale gradient in the following manner:

$$R \frac{U_{av}}{L_j} \propto \frac{U_\lambda - U_\beta}{L_\lambda}. \quad (4.10)$$

By combining (4.9) and (4.10), R may be estimated using measured velocities:

$$R = \frac{-(U_\beta - U_\lambda)^2}{U_{av}(U_{av} - U_\beta)}, \quad (4.11)$$

where U_λ and U_β are determined from the instantaneous maximum and minimum velocities measured across the core of the jet ($0 < \eta < 1$). Using velocities measured near the jet midplane ($z/H = 0.56$), we estimate an average R value of 1.5. We divided the meander removed values of $-\overline{u'v'}$ by the R adjusted time-averaged values of $\partial U/\partial y$ to calculate the non-meander influenced diffusivities presented in figure 14. When the lower-frequency large-scale turbulence is removed from the time series, momentum diffusivities decrease on average by a factor of 300 in the near-surface layer and a factor of 100 in the near-bed layer (figure 14). The majority of this decrease results from the reduction in lateral shear stress when the influence of the meandering structure is removed from the turbulence (figure 13).

4.5. Momentum

Momentum should be conserved in a self-similar jet (Tennekes & Lumley 1972). Review of prior studies by Giger *et al.* (1991), however, indicates that momentum conservation is infrequently observed in jet experiments. In wall-bounded jets momentum will also be lost via bed friction. A number of theoretical treatments of wall-bounded jets have attempted to account for momentum loss due to bed friction (Borichansky & Mikhailov 1966; Ozsoy 1977; Joshi 1982; Ozsoy & Unluata 1982; Wang 1984) and the experiments of Giger *et al.* (1991) clearly show the effect of bed friction on the loss of momentum in bounded plane jets. To evaluate the potential influence of bed friction on our experimental jet we made two estimates of the momentum (M), relative to the initial outlet momentum (M_o), for each measurement section across the ZOEF. The first estimate, $\overline{U}^2 W$, was made based on the measured mean streamwise velocities (\overline{U}) and the total width of the measurement section (W). These estimates underestimate the actual momentum because velocity profiling did not extend fully to the outermost margins of the jet.

The second approach follows the analysis of Giger *et al.* (1991) in which the momentum at any cross-section of the jet may be estimated assuming self-similarity of the jet velocity structure:

$$M = U_m^2 b I, \quad (4.12)$$

where I represents the integral solution for f^2 between the margins ($-\eta_B$ to η_B) of the jet

$$I = \int_{-\eta_B}^{\eta_B} f^2 d\eta, \quad (4.13)$$

and has a value of 1.49 when f is represented by (4.4) (Giger *et al.* 1991). Using (4.12) and (4.13) and the experimentally determined spreading rates for velocity (C_u) and half-widths (C_b), and the respective virtual origins, Giger *et al.* (1991) show that the ratio of momentum to initial momentum may be calculated with the following relationship:

$$\frac{M}{M_o} = I \frac{C_b \xi - \xi_b}{C_u \xi - \xi_u}. \quad (4.14)$$

Relative momentum (M/M_o) estimated from measured velocities are presented (data points) along with values calculated by (4.14) (solid lines) across the ZOEF in figure 15. The estimates based on measurements all fall below those of (4.14) due to

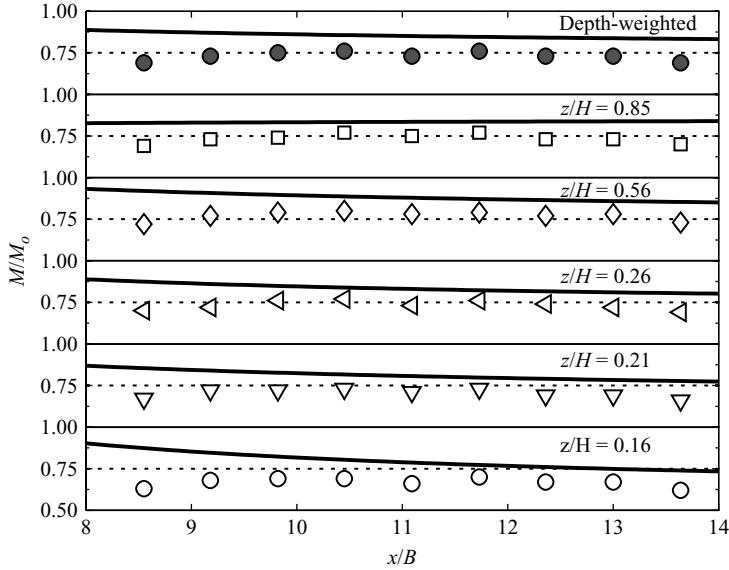


FIGURE 15. Estimates of momentum (M) relative to initial momentum at the outlet (M_o) across the ZOEF. Symbols represent estimates based on measured streamwise velocity cross-sections and solid lines represent (4.14).

the incomplete profiling. Both estimates, however, show two trends: (i) momentum loss increases with proximity to the bed and (ii) the rate of momentum loss in the downstream direction increases with proximity to the bed. The relatively constant values of (M/M_o) in the upper half of the flow suggest that most of the momentum loss in these layers occurs across the ZOFE, while closer to the bed momentum loss continues across the ZOEF.

5. Discussion

5.1. Vertical variations in cross-stream structure

The mean structure of streamwise velocity and the magnitudes of turbulence intensities in our experimental jet are in close agreement with prior experiments on plane jets across the depth of the flow. Near the upper free surface of the jet, the distributions and relative magnitudes of the cross-stream velocities, the lateral shear stresses and the diffusivity of lateral momentum are also in general agreement with expected values for self-similar plane jets. With proximity to the bed, however, these properties show increasing deviation in both distribution and magnitude from that of a self-similar plane jet.

The vertical gradient in cross-stream velocities we observe (figure 9) are not inconsistent with prior observations of wall-bounded plane jets. Giger *et al.* (1991) and Dracos *et al.* (1992) observed higher entrainment rates of ambient fluid into shallow jets along the midplane of jets bounded by solid walls at both the upper and lower surfaces. This vertical variation in the influx of low momentum fluid suppressed velocity and spreading rates along the midplane relative to the flow nearer the walls (Dracos *et al.* 1992). If a similar effect is present in our experiments it may provide an explanation for the observed reduction in near surface velocities relative to those near the mid depth of our jet (figure 7).

Both in the experiments of Giger *et al.* (1991) and Dracos *et al.* (1992) as well as earlier experiments on wall-bounded jets by Foss & Jones (1968) and Holdeman & Foss (1975) the complex interaction of bed-generated turbulence with lateral shear-generated turbulence led to the development of secondary circulation cells due to the horizontal rotation of initially vertically oriented vortices generated by lateral shear stress. Foss & Jones (1968) and Holdeman & Foss (1975) observed that such cells decayed by distance of $x/B \sim 40$. Giger *et al.* (1991) and Dracos *et al.* (1992) did not observe the development of these structures in their shallowest experiments ($H/B = 0.25$) and found in experiments where they did occur that such structures rapidly decayed by distances of $H/B \sim 10$. We lack vertical velocity measurements across the entire flow depth of our jet to evaluate the presence or absence of such flow structures in our work, but based on these prior studies it would appear to be an unlikely explanation for our results given the width of our jet and the persistence of turbulence structures observed.

We lack a definitive explanation for observed vertical variation in cross-stream velocity, lateral shear and momentum diffusivity. Three possible causes include (i) data collection errors and/or near-bed velocity probe interference, (ii) influence of the unique experimental outlet channel geometry or (iii) bottom boundary influence on the jet. Without additional experimental runs and measurements with non-intrusive instrumentation it is not possible to definitively rule out data collection errors or probe interference. Reproducibility of vertical profiles, measurement errors (3%) far less than the observed variability and consistency of repeated near-bed velocity measurements, however, suggest that there is no systematic measurement error associated with flow depth. Further, the possible interference of the probe on velocity measurements, such as an instrument wake, is highly unlikely due to its position cross-stream of the sampling volume and such an effect should not have a dependence on proximity to the bottom boundary (the meandering structure is present at all flow depths). Finally, video of the flow, collected at the jet boundaries confirms that vertical variations in cross-stream flow, seen in figure 9, occur and vary with passage of the meandering structure.

Given the partial, but diminishing, confinement of the jet over the first 1 m of flow into the experimental basin, it is possible that the vertical structure in lateral entrainment observed along the jet develops from these outlet conditions. If this is the cause, the persistence of the observed structures down jet would imply that the flow patterns developed along this channel remain largely unchanged even in the absence of lateral walls downstream of the channel. While this potential cause cannot be ruled out with the available data, the development of such a persistent circulation pattern of flow into the jet would be in contrast to prior observations that secondary circulation cells in bounded plane jets are short-lived structures that rapidly decay in the downstream direction (e.g. Foss & Jones 1968; Holdeman & Foss 1975; Giger *et al.* 1991; Dracos *et al.* 1992). Regardless of the exact mechanism, if our observations are the result of the experimental set-up they highlight a potentially important deviation in jet structure between prior experimental works on jets with abrupt outlet conditions and conditions at river and tidal outlets, partially bounded by subaqueous deposits, that undergo a transition between confined to fully unconfined flow over a distance of several channel widths.

Prior works on wall-bounded jets (e.g. Foss & Jones 1968; Holdeman & Foss 1975; Giger *et al.* 1991; Dracos *et al.* 1992) report the effects of bed-generated turbulence on cross-stream velocity structure and secondary circulation patterns, but none examine lateral shear stresses or momentum diffusivity. Our observed deviation in lateral shear

stresses and momentum diffusivities may reflect an additional effect of bed-generated turbulence on structure of wall-bounded jets.

5.2. Experimental implications for river and tidal settings

Large-scale meandering turbulent structures are well documented in shallow mixing layers (for review see Jirka 2001). In the case of shallow jets, these structures have been shown to significantly influence local mixing, entrainment and dispersal of scalars (Giger *et al.* 1991; Dracos *et al.* 1992; Jirka 2001). The decomposition of our jet into meander and bed-generated turbulence clearly shows the dominance of the meandering structure on turbulence intensities and confirms the suggestion of Jirka (2001) that such structures have a significant influence on the lateral exchange of momentum. Our results suggest that analysis and models of flow systems such as tie channels, river outlets and tidal jets with these large-scale instabilities need to incorporate the effect of these structures to accurately predict turbulence and mixing. For example, a common approach to estimating the transverse eddy viscosity in wide shallow flows ($\nu_t = 0.13Hu_*$, where u_* is the shear velocity, Fischer 1973) under predicts the momentum diffusivity in our jet by two orders of magnitude. This approach, however, does provide a reasonable estimate for the momentum diffusivities once the influence of large-scale meander is removed from the turbulence.

While systems with large-scale meandering structures, such as tie channels and tidal jets are common, our review of aerial photographs and satellite imagery of flows from river mouths into open water suggests that these large-scale structures are not ubiquitous features in coastal and lacustrine settings. Linear stability analysis of coherent structures in shallow mixing layers (Jirka 1994, 2001; Chen & Jirka 1997; vanProoijen & Uijttewaai 2002; Socolofsky & Jirka 2004) suggests a strong aspect ratio dependence on the development of these large-scale structures. Such analysis indicates that the development of the large-scale instabilities depends on the jet Reynolds number ($Re_j = U_m b / \nu_t$) and a stability parameter (S) (Jirka 1994). In most, if not all, river or tidal settings jet flow may be treated as inviscid and the development of large-scale instabilities becomes a function of the stability parameter alone. The stability parameter varies by a factor of two between researchers (Jirka 2001; vanProoijen & Uijttewaai 2002; Socolofsky & Jirka 2004), depending on assumptions regarding ν_t , but takes the general form

$$S = \frac{c_f B}{2 H}. \quad (5.1)$$

As aspect ratio (B/H) and bed friction increase at river mouths or tidal outlets the likelihood of large-scale meandering structures decreases. Based on a critical stability value of 0.12 (vanProoijen & Uijttewaai 2002) and the range of c_f values estimated for our experiment, the meandering structure in our experiments would be expected to be suppressed if either the aspect ratio (B/H) or bed friction were increased by a factor of 7–13. How such a change in the turbulence structure of the jet would influence the mean streamwise velocity structure of the jet cannot be predicted from our experiments. Our comparison of meander-dominated versus bed-dominated turbulence, however, suggests that the overall turbulence intensities and lateral momentum transfer would be greatly reduced in these settings and may deviate significantly from predictions based on existing plane jet theory.

Our experiments were conducted under static morphological conditions. In tidal and river settings the combination of bed-erosion and the deposition of subaqueous levees may have important feedbacks on hydrodynamics. In the case of our prototype tie

channels, field data (Rowland *et al.* in press) indicates the rates of bed deformation (due to both erosion and deposition) and levee development occur at time scales much greater than the flow time scales examined in our experiments. As such our experimental results likely give reasonable picture of the channel hydrodynamics. In other settings, such as tidal inlets, with highly deformable beds and rapidly varying flow depths, flow and turbulence conditions, however, may change from one dominated by plane jet characteristics to that largely controlled by bed-friction over the course of a single flow event. In such cases, our results highlight the possible range in turbulence intensities, lateral shear stresses and momentum transfer that may be expected both temporally and vertically. Our results, however, do not offer a simple modification to semi-empirical numerical models to address these variations. Given the significant near-bed deviations in lateral shear and momentum transfer we observe (from either our outlet conditions or the influence of bed friction), our results suggest morphodynamics models that seek to couple jet hydrodynamics to sediment transport need to be able to explicitly account for interactions between bed-generated turbulence and large-scale quasi-two-dimensional turbulent structures.

6. Conclusions

Our experimental results provide one of the few tests of experimentally and theoretically derived solutions for plane jet dynamics in inertially driven channel flow that enters quiescent waters. Importantly, our experimental flows had aspect ratios similar to that found in nature and had a solid bed and a free water surface. We find that at distances greater than nine channel widths from the jet outlet, the mean velocity structure, streamwise velocity decay, spreading rates and turbulence intensities agree with existing plane jet theory. Near the upper free surface, magnitudes and distribution of the cross-stream velocity, lateral shear stresses and lateral diffusivity of momentum also agree well with results of prior plane jet studies.

With proximity to the bottom bounding wall, however, the distributions and magnitudes of cross-stream velocities, lateral shear stresses and lateral momentum diffusivities increasingly deviate from self-preserving characteristics of unbounded plane jets. Lateral shear stresses and momentum diffusivities decrease on average by an order of magnitude from the upper free surface to near the bed. While we believe that our data suggest a limited influence of our particular (but not unrealistic) outlet conditions on the structure of the jet, we cannot definitively rule out its role on the vertical variations in jet structure we observe. Irrespective of the cause, however, our results suggest that in models of river mouth or tidal outlet hydrodynamics, where flow is in contact with the bed and partially constrained by subaqueous deposits, significant vertical variations in the turbulent structure of jets may need to be taken into account.

Finally, analysis of the turbulent structure both with and without the influence of the lower-frequency quasi-periodic meandering turbulent structure indicates that this lateral shear-induced instability dominates the turbulence of the jet. Analysis of velocity time series with this structure removed indicates that the turbulence intensities decrease by 3–5 times and the lateral shear stresses and momentum diffusivities drop by one and two orders of magnitude, respectively.

This work was supported by funding from the American Chemical Society Petroleum Research Fund and the National Center for Earth-Surface Dynamics (NCED). We thank Jeremy Venditti, Kathleen Mai and Timothy Greib for assistance

in data collection and analysis. Stuart Foster, John Potter and Neto Santana all provided critical assistance in flume construction. We also thank Chris Ellis at the Saint Anthony Falls Laboratory, University of Minnesota who freely gave his insights and advice on experimental design. The manuscript greatly benefitted from thoughtful and thorough reviews by G. Seminara and two anonymous reviewers.

REFERENCES

- ABRAMOVICH, G. N. 1963 *Theory of Turbulent Jets*. MIT Press.
- AGRAWAL, A. & PRASAD, A. K. 2003 Integral solution for the mean flow profiles of turbulent jets, plumes, and wakes. *J. Fluids Engng* **125** (5), 813–822.
- ALBERTSON, M. L., DAI, Y. B., JENSEN, R. A. & ROUSE, H. 1950 Diffusion of submerged jets. *Trans. Am. Soc. Civil Engineers* **115**, 639–664.
- BATES, C. C. 1953 Rational theory of delta formation. *AAPG Bull.* **37** (9), 2119–2162.
- BIRON, P., ROY, A. G. & BEST, J. L. 1995 A scheme for resampling, filtering, and subsampling unevenly spaced laser-doppler anemometer data. *Math. Geol.* **27** (6), 731–748.
- BORICHANSKY, L. S. & MIKHAILOV, V. N. 1966 Interaction of river and sea water in the absence of tides. In *Scientific Problems of the Humid Tropical Zone Deltas and their Implications*, pp. 175–180. UNESCO.
- BRADBURY, L. J. S. 1965 The structure of a self-preserving turbulent plane jet. *J. Fluid Mech.* **23** (1), 31–64.
- CHEN, D. Y. & JIRKA, G. H. 1997 Absolute and convective instabilities of plane turbulent wakes in a shallow water layer. *J. Fluid Mech.* **338**, 157–172.
- DRACOS, T., GIGER, M. & JIRKA, G. H. 1992 Plane turbulent jets in a bounded fluid layer. *J. Fluid Mech.* **241**, 587–614.
- EDMONDS, D. A. & SLINGERLAND, R. L. 2007 Mechanics of middle-ground bar formation: implications for the morphodynamics of delta distributary networks. *J. Geophys. Res.-Earth Surf.* **112**.
- FISCHER, H. B. 1973 Longitudinal dispersion and turbulent mixing in open-channel flow. *Annu. Rev. Fluid Mech.* **5**, 59–78.
- FOSS, J. F. & JONES, J. B. 1968 Secondary flow effects in a bounded rectangular jet. *J. Basic Engng* **90** (2), 241–248.
- GIGER, M., DRACOS, T. & JIRKA, G. H. 1991 Entrainment and mixing in plane turbulent jets in shallow-water. *J. Hydraulic Res.* **29** (5), 615–642.
- HOLDEMAN, J. D. & FOSS, J. F. 1975 Initiation, development, and decay of secondary flow in a bounded jet. *J. Fluids Engng-Trans. Asme* **97** (3), 342–352.
- IZUMI, N., TANAKA, H. & DATE, M. 1999 Inceptive topography of fluvial-dominated river mouth bars. In *River Sedimentation* (ed. Lee & Wang). Balkema.
- JIRKA, G. H. 1994 Shallow jets. In *Recent Research Advances in the Fluid Mechanics of Turbulent Jets and Plumes* (ed. P. A. Davies & M. J. Valente Neves), pp. 155–175. Kluwer Academic Publishers.
- JIRKA, G. H. 2001 Large scale flow structures and mixing processes in shallow flows. *J. Hydraulic Res.* **39** (6), 567–573.
- JOSHI, P. B. 1982 Hydromechanics of tidal jets. *J. the Waterway Port Coastal Ocean Div.-ASCE* **108** (3), 239–253.
- KOSTASCHUK, R. A. 1985 River mouth processes in a fjord-delta, British Columbia, Canada. *Marine Geol.* **69** (1–2), 1–23.
- LANE, S. N., BIRON, P. M., BRADBROOK, K. F., BUTLER, J. B., CHANDLER, J. H., CROWELL, M. D., MCLELLAND, S. J., RICHARDS, K. S. & ROY, A. G. 1998 Three-dimensional measurement of river channel flow processes using acoustic doppler velocimetry. *Earth Surf. Processes Landforms* **23** (13), 1247–1267.
- OLD, C. P. & VENNEL, R. 2001 Acoustic doppler current profiler measurements of the velocity field of an ebb tidal jet. *J. Geophys. Res.-Oceans* **106** (C4), 7037–7049.
- OZSOY, E. 1977 Flow and mass transport in the vicinity of tidal inlets. *Tech. Rep.* TR-036. University of Florida, Coastal and Oceanographic Engineering Laboratory.

- OZSOY, E. & UNLUATA, U. 1982 Ebb-tidal flow characteristics near inlets. *Estuarine Coastal Shelf Sci.* **14** (3), 251–263.
- VANPROOIJEN, B. C. & UIJTTEWAAL, W. S. J. 2002 A linear approach for the evolution of coherent structures in shallow mixing layers. *Phys. Fluids* **14** (12), 4105–4114.
- REICHARDT, H. 1942 Gesetzmäßigkeiten der freien turbulenz. *VDI—Forschungsheft* 414.
- ROWLAND, J. C. 2007 Tie channels. PhD thesis, University of California, Berkeley.
- ROWLAND, J. C. & DIETRICH, W. E. 2006 The evolution of a tie channel. In *River, Coastal and Estuarine Morphodynamics: RCEM 2005* (ed. G. Parker & M. H. Garcia), pp. 725–736. Taylor & Francis.
- ROWLAND, J. C., DIETRICH, W. E., DAY, G. & PARKER, G. In press. The formation and maintenance of single-thread tie channels entering floodplain lakes: observations from three diverse river systems. *J. Geophys. Res.—Earth Surf.*
- ROWLAND, J. C., LEPPER, K., DIETRICH, W. E., WILSON, C. J. & SHELDON, R. 2005 Tie channel sedimentation rates, oxbow formation age and channel migration rate from optically stimulated luminescence (OSL) analysis of floodplain deposits. *Earth Surf. Processes Landforms* **30** (9), 1161–1179.
- SCHLICHTING, H. 1968 *Boundary-Layer Theory*, 6th ed. McGraw-Hill Book Company.
- SEO, I. W. & KWON, S. J. 2005 Experimental investigation of three-dimensional nonbuoyant rectangular jets. *J. Engng Mech.* **131** (7), 733–746.
- SOCOLOFSKY, S. A. & JIRKA, G. H. 2004 Large-scale flow structures and stability in shallow flows. *J. Environmental Engng Sci.* **3** (5), 451–462.
- SYVITSKI, J. P., SKENE, K. I., NICHOLSON, M. K. & MOREHEAD, M. D. 1998 Plume1.1: deposition of sediment from a fluvial plume. *Comput. Geosci.* **24** (2), 159–171.
- TENNEKES, H. & LUMLEY, J. L. 1972 *A First Course in Turbulence*. The MIT Press.
- TOLLMIE, W. 1926 Berechnung turbulenter ausbreitungsvorgänge. *Zeitschrift für Angewandte Mathematik und Mechanik* **6**, 468–478.
- TOWNSEND, A. A. 1976 *The Structure of Turbulent Shear Flow*, 2nd edn. Cambridge University Press.
- WANG, F. C. 1984 The dynamics of a river-bay-delta system. *J. Geophys. Res.—Oceans* **89** (NC5), 8054–8060.
- WRIGHT, L. D. 1977 Sediment transport and deposition at river mouths – synthesis. *Geol. Soc. Am. Bull.* **88** (6), 857–868.
- WRIGHT, L. D. & COLEMAN, J. M. 1974 Mississippi river mouth processes – effluent dynamics and morphologic development. *J. Geol.* **82** (6), 751–778.